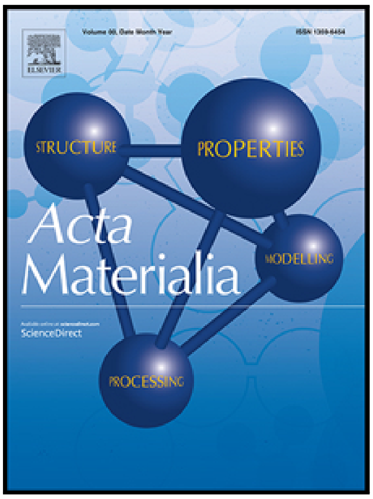

Copper Diffusion Rates and Hopping Pathways in Superionic Cu_2Se

Sheik Md Kazi Nazrul Islam , Prince Mayank , Yulou Ouyang ,
Jie Chen , Arun. K. Sagotra , Meng Li , Michael B. Cortie ,
Richard Mole , Claudio Cazorla , Dehong Yu , Xiaolin Wang ,
Robert A. Robinson , David Laurence Cortie

PII: S1359-6454(21)00406-7
DOI: https://doi.org/10.1016/j.actamat.2021.117026
Reference: AM 117026

To appear in: *Acta Materialia*

Received date: 13 October 2020
Revised date: 30 April 2021
Accepted date: 24 May 2021

Please cite this article as: Sheik Md Kazi Nazrul Islam , Prince Mayank , Yulou Ouyang , Jie Chen , Arun. K. Sagotra , Meng Li , Michael B. Cortie , Richard Mole , Claudio Cazorla , Dehong Yu , Xiaolin Wang , Robert A. Robinson , David Laurence Cortie , Copper Diffusion Rates and Hopping Pathways in Superionic Cu_2Se, *Acta Materialia* (2021), doi: https://doi.org/10.1016/j.actamat.2021.117026

Copper Diffusion Rates and Hopping Pathways in Superionic Cu_2Se

Sheik Md Kazi Nazrul Islam[1,2], Prince Mayank[3], Yulou Ouyang[4], Jie Chen[4], Arun. K. Sagotra[5], Meng Li[1], Michael B. Cortie[2], Richard Mole[6], Claudio Cazorla[5], Dehong Yu[6], Xiaolin Wang[1], Robert A. Robinson[1], David Laurence Cortie[*1]

[1] The Institute for Superconducting and Electronic Materials, Australian Institute for Innovative Materials, University of Wollongong, North Wollongong, NSW 2500, Australia

[2] School of Mathematical and Physical Sciences, University of Technology Sydney, Broadway, NSW 2007, Australia

[3] Indian Institute of Technology Delhi, New Delhi 110016, India

[4] Center for Phononics and Thermal Energy Science, China-EU Joint Lab for Nanophononics, School of Physics Science and Engineering, Tongji University, Shanghai 200092, China

[5] School of Materials Science and Engineering, University of New South Wales, Sydney, 2052, Australia

[6] The Australian Nuclear Science and Technology Organisation, Lucas Heights, NSW 2232, Australia

* dcortie@uow.edu.au

Keywords: copper selenide, neutron scattering, molecular-dynamics, thermoelectricity

Abstract

The ultra-low thermal conductivity of Cu_2Se is well established, but so far there is no consensus on the underlying mechanism. One proposal is that the fast-ionic diffusion of copper suppresses the acoustic phonons. The diffusion coefficients reported previously, however, differ by two orders of magnitude between the various studies and it remains unclear whether the diffusion is fast enough to impact the heat-bearing phonons. Here, a two-fold approach is used to accurately re-determine the diffusion rates. *Ab-initio* molecular dynamics simulations, incorporating landmark analysis techniques, were closely compared with experimental quasielastic/inelastic neutron scattering. Reasonable agreement was found between these approaches, consistent with a diffusion coefficient of $3.1 \pm 1.3 \times 10^{-5}$ $cm^2.s^{-1}$ at 675 K and an activation barrier of 140 ± 60 meV. The hopping mechanism includes short 2 Å

hops between tetrahedral and interstitial octahedral sites. This process forms dynamic Frenkel defects. Despite the latter processes, there is no major loss of the phonon mode intensity in the superionic state, and there is no strong correlation between the phonon spectra and the increased diffusion rates. Instead, intrinsic anharmonic phonon interactions appear to dictate the thermal conductivity above and below the superionic transition, and there is only subtle mode broadening associated with the monoclinic-cubic structural transition point, with the phonon density-of-states remaining almost constant at higher temperatures.

1. Introduction

Liquids have almost no resistance to transverse shear stresses and this permits them to flow freely at the macroscopic scale. For a similar reason, the transverse elastic waves in a liquid are strongly suppressed, at least at long wavelengths. This is reflected in the reduction of the heat capacity from the Dulong-Petit law to below the standard value found in solids ($C_v \sim 3k_BN$) [1]. A subject of great interest is the situation in superionic conductors, which constitute an unusual class of matter with features of both solids and liquids. In such materials (e.g. β-Cu_2Se), one atomic species (Cu) undergoes rapid ionic diffusion, whereas the other species (Se) forms a stable crystal lattice [1]. These rare compounds generally feature mobile silver, lithium or copper ions in spacious crystal structures, and they have attracted interest as potential solid electrolytes for battery technology. The anomalously low thermal conductivity found in some superionic semiconductors also enables superb thermoelectric performance. For example, β-Cu_2Se offers a thermoelectric figure-of-merit (zT) in the range 1.0 to 2.5 which approaches the highest values ever reported for any thermoelectric [2]. This is linked to the “phonon-liquid-electron-crystal” state, which offers low thermal conductivity in tandem with high electrical conductivity [1]. Yet the origin of this novel state, and its connection with the superionic behavior, is still debated [3].

One theory is that this is a direct consequence of the rapid diffusion of copper in the superionic phase, which has an onset at 405 to 410 K, the temperature at which stoichiometric α-Cu_2Se transforms to β-Cu_2Se [1, 4]. By analogy to liquids, it was proposed that copper motion suppresses the transverse phonons, thereby reducing the thermal conductivity [1]. However, the role of the rigid Se lattice is yet to be clarified. An alternative hypothesis is that strongly anharmonic cation-anion interactions are the critical factor as this causes increased phonon scattering across a broader temperature range, independently of the diffusion behavior [3]. This general question has been raised in several related materials [5, 6]. The apparent deviation from the Dulong-Petit law at high temperature in Cu_2Se may favor the first viewpoint although the measurements of heat capacity do differ between different studies [1, 7]. On the other hand, a recent inelastic neutron scattering study concluded that the phonon spectrum is effectively constant from 300 – 900 K whilst the copper diffusion coefficient is low [3]. However, the diffusion coefficients determined in the latter work differ by two orders of magnitude from the earlier determinations by Danilkin *et al.*[8, 9] and Horvatić *et al.*[10, 11]. The latter also reported that the value depends critically on the Cu stoichiometry in $Cu_{2-x}Se$. Clearly, further work is required to resolve these issues.

Here we report experimental neutron scattering data and *ab-initio* molecular-dynamics simulations (AIMD), and provide some simple geometrical arguments to support a unified model for copper diffusion in Cu_2Se. Our neutron data are similar to those reported by others, but we show that the data is complex to interpret, and our conclusions are different. Essentially, while it is not possible to distinguish between two hopping pathways with frequencies that are both similar in energy scale to the resolution of the experiment, it is possible to place upper and lower bounds. The AIMD is much more definitive and there is very clear evidence for a major role involving tetrahedral–octahedral and tetrahedral–tetrahedral site hops. This is supported by geometrical arguments resulting from the intrinsic structure of the anti-fluorite lattice, as well as X-ray diffraction data. The model is qualitatively different from those previously proposed for diffusion in Cu_2Se, and for the first time, we end up with a unified self-consistent picture that respects the evidence from simulation, neutron scattering, and the measured bulk *T*-dependent diffusion constants. Furthermore, this model self-consistently explains the intrinsic hopping mechanism in stoichiometric Cu_2Se without the need for Cu vacancies, which remained unexplained in past models. It also correctly reproduces the overall vibrational density of states.

2. Methods

Theoretical: AIMD simulations and nudged-elastic band calculation (NEB) were performed using density functional theory (DFT) in the Vienna Ab Initio Simulation Package (VASP) [12-14]. To analyze the ionic transport properties of Cu_2Se, simulations were performed in the canonical ensemble (N,V,T) using the generalized gradient approximation (GGA) to the exchange-correlation energy due to Perdew *et al.* (GGA-PBE). The projector augmented-wave method was used to represent the ionic cores [12-14], and the electronic states Cu 4s-3d and Se 4s-4p were considered as valence. Wave functions were represented in a plane-wave basis and the cut-off energy was 500 eV. To model the effect of Cu vacancies in $Cu_{2-x}Se$, additional simulations were performed by removing a single copper atom from the cell.

Landmark decomposition of the molecular dynamics: Landmark analysis of the DFT results was performed to accurately track the ionic motion of Cu through the lattice, and extract residence times for the different types of Cu hopping motions. Two variants of landmark analysis were performed: one using spherical landmarks, and one using Voronoi landmarks using the recently developed SITATOR toolkit developed by Kahle *et al.* for “unsupervised” Voronoi landmark analysis [15]. Further detail on the DFT and landmark analysis is given in the supplementary material.

Visualization of the molecular dynamics and corresponding neutron spectral functions: The Visualization for Electronic and Structural Analysis (VESTA) software was used to plot the average structure and copper density maps [16]. VMD was used to plot the trajectories and time-lapse images from the molecular dynamics simulations [17]. The MD trajectories were used to simulate the neutron spectroscopy dataset by deploying the approach implemented in the nMoldyn (v3) software [18-20].

*Experimental***:** Commercially obtained Cu_2Se (99.99%) was crushed into a fine powder and processed by spark plasma sintering (SPS; Thermal Technology SPS model 10-4) at 772 K for 10 min under a pressure of 40 MPa in a vacuum. Inelastic neutron scattering experiments were conducted on the PELICAN time-of-flight neutron spectrometer [21] at the Australian Nuclear Science and Technology Organisation. The Cu_2Se powder sample was placed in an annular aluminum sample can. The instrument was optimized for scans using λ = 4.74 Å incident neutrons, affording energy resolutions approximated by a Gaussian full-width-at-half-maximum (FWHM) of 135 μeV at the elastic line. Complementary high-temperature X-ray powder diffraction was conducted at the Australian Synchrotron at a wavelength of λ = 0.58973 Å. Thermal conductivity was measured by the laser flash method using a Linseis LFA 1000. Further experimental details are provided in the supplementary material.

3. Results

3.1. Geometric analysis

Copper selenide possesses the anti-fluorite structure, with the Fm-3m spacegroup (#225), as illustrated in Fig. 1. The structure is identical to the fluorite structure (e.g. CaF_2) except that the anion and cation sites are reversed. The selenium atoms form a rigid lattice and occupy the *a*-Wyckoff site at the (0,0,0) and symmetry-equivalent positions. The mobile copper atoms have their highest occupancy at the tetrahedral "T-sites", the *c*-Wyckoff position, with fractional coordinates (1/4, 1/4, 1/4). For long-range diffusion to occur, Cu must navigate between the various T-sites. Assuming the jumps occur directly between the T-sites, the hopping vectors are shown in Fig. 1(a) with the nearest-neighbor hop corresponding to ~ 3 Å. We label these as T↔T transitions. Recent work has focused exclusively on the role of T↔T transitions for mediating diffusion [3]. However, several past XRD and near-edge X-ray absorption spectroscopy (NEXAFS) studies have also identified that a smaller fraction of the Cu occupies the interstitial octahedral "O-sites" [8, 9]. The lightly-occupied O sites are, on average, centered on 8b site at the (½, ½, ½) position, although some reports may indicate they are slightly offset (e.g. ½±δ, ½±δ, ½±δ, within the closely related 32f sites). In either case, if these O-sites are included in the Cu network, this enables a new set of hopping pathways as illustrated in Fig. 1(b) which include shorter hopping vectors ~ 2 Å. We label these as T↔O transitions. The hop from T→O can be considered to generate a Frenkel defect pair [22], consisting of the vacant tetrahedral site, and the copper in the interstitial O-site. Long-range diffusion via T↔O transitions is also possible because a T→O transition followed by an O→T transition can move a Cu away from its original T-site to a neighboring tetrahedral vacancy. To assess the likelihood of T↔O versus T↔T transitions, an analysis of the steric hindrance for different hopping vectors is presented in Table I. This shows that the closest-approach for a Cu-Se pair is 0.354a for a T↔T jump, where a is the cubic lattice constant. In contrast, T↔O hops allow for greater clearance between the Cu-Se pairs (0.408a). Intuitively T↔O transitions, therefore, seem very likely, given the larger channel width, yet the octahedral and tetrahedral environments are quite different (Fig. 1(c) and (d)) and thus the internal energy differences may make one of the sites unstable, or metastable. To confirm the latter points, density-functional theory calculations were performed to compare the T→O and T→T activation barriers, using the nudged elastic band method. The results are shown in Fig. 1(e) and (f). As anticipated, the T→O transition has a significantly lower barrier (0.2 eV) compared to the T→T transition (0.4 eV). Furthermore, the octahedral site appears as a metastable point in the pathway. This explains the low occupancy found on the O-site experimentally. Consequently, if any T→O transition occurs, it will generally be followed by a subsequent O→T transition, and the Frenkel defects will be short-lived and dynamic. Nevertheless, the short-lived vacancy generated by an O→T transition is an important mechanism to allow hopping and avoid double occupancy on the tetrahedral copper sites. For example, if one assumes that 1% of the T- sites contain dynamic or extrinsic vacancies, there is a 23% chance that a Cu which undergoes a T→O hop can find a different tetrahedral vacancy available for its next O→T hop. A more detailed explanation of the underlying statistical argument is given in the supplemental materials. One important consequence is that this analysis naturally explains how copper can hop in stoichiometric Cu_2Se *without any extrinsic copper vacancies* because the T↔O hops dynamically generate the vacancies required to avoid a "Cu traffic jam" on the T-site, allowing Cu to shuffle past each other using the O-site as a bypass. In the following sections, we discuss molecular dynamics calculations and quasielastic neutron scattering (QENS) measurements which reveal that the latter picture is essentially correct, and that T↔O transitions dominate overall.

Table I. Summary of nearest Cu-Se hopping distances, vectors and closest approach distances in terms of the cubic lattice constant (a), as expressed in Ångstroms, assuming a = 5.83 Å.

Label	Description	Closest approach for Cu-Se pair	Hopping distance between sites
$(T\text{-}T)_i$	Hopping along <100> directions between nearest-neighbor T-sites positions	0.354 *a*	0.5 *a* = *2.92 Å*
$(T\rightarrow T)_{ii}$	Hopping along <110> directions, between next-nearest neighboring tetrahedral to tetrahedral sites.	0.250 *a*	0.7 *a* = *4.13 Å*
T↔O	Hopping along <111> directions between tetra-octa sites	0.408 *a*	0.43 *a* = *2.529 Å*
O→O	Hopping along <110> directions from octahedral to octahedral sites.	0.354 *a*	0.7 *a* = *4.13 Å*

3.2 Ab-Initio Molecular Dynamics

Ab-initio molecular dynamics simulations are a powerful tool to study the motion of an ensemble of Cu and Se atoms self-consistently, with a realistic depiction of the internal energy landscape and atomic forces including anharmonic interactions. For Cu_2Se, AIMD simulations show that both the Se and Cu sublattices are thermally agitated and that the atoms move considerable distances from their idealized position, as illustrated in the time-lapse image taken at 700 K in Fig. 2 which shows the same features identified in past work [23]. In agreement with experiment, the simulations also predict long-range ionic diffusion for the Cu, whereas the Se atoms are trapped near their initial site positions (below 900 K). The mean-squared displacements of the Cu during the simulation (Fig. 3(a)) indicate long-range diffusion, where the slope is related to the diffusion coefficient via the Einstein relation:

$$D = lim_{\tau\to\infty} \frac{MSD(\tau)}{6\tau} \tag{1}$$

The error bars for the mean-squared displacements were estimated using the method discussed in Ref [24]. The values for the diffusion coefficients show good agreement with the most reliable experimental values, as discussed in detail later.

Close inspection of the MD also reveals that the individual Cu ions experience three main types of atomistic hopping. To illustrate this, Fig. 3(b) displays a representative trajectory for a single Cu as a time-lapse image. Firstly, the Cu atom undergoes frequent T↔O transitions described in the earlier section, corresponding to hops mainly along the <111> directions. The Cu in the O-site has a finite residency time, indicating that it is a metastable site. Secondly, at high temperature, the Cu occasionally hops directly between tetrahedral sites (i.e. T↔T transitions), involving hopping along a <100> direction. Thirdly, the Cu sometimes dwells for longer times in the T/O sites, undergoing confined local diffusion, orbiting to further distances around the average Wyckoff position, within what is still a fairly large “interstitial “cage”.

This motion occurs even at a lower temperature when the Cu atoms are not undergoing long-range diffusion. The dynamics for the T↔O and T↔T are consistent with the earlier description in Table I and Fig. 1. The only caveat is that the confined diffusion around the T/O-sites introduces a thermal spread of copper positions in the sites, which in turn means that hops are not simply parallel to <111> or <100> or exactly 2 or 3 Å, but rather distributed around these average values. As the number of events per Cu is relatively low, it can be misleading to examine a single atom since there is a large statistical variation. Landmark analysis of the entire ensemble is, therefore, a better tool to extract the average behavior.

In the simplest approach, landmarks were manually placed at the T- and O-sites throughout the supercell, where the positions were as defined in the time-averaged structure. As detailed in the supplementary material, any Cu atom within d_0 = 1 Å of a landmark site was labelled with that site's unique ID and type (O or T), and transitions could be tracked by monitoring the site IDs for each atom at each frame (for example, shown in Fig. 3(c)). By performing this procedure for all 144 Cu atoms in the simulation, the average residence time and transition rates between types were extracted. Table II presents the average transition rates, at 700 K, for the entire copper ensemble, along with the statistical analysis of the various hopping events. The fractions of the different types of hops extracted is fairly robust, since it did not depend on the cutoff radius d_0, but the residence times were found to depend strongly on the choice of cut-off size. This reflects that the choice of the spatial region defining a site is somewhat arbitrary, and the copper also spends a considerable amount of time in 'no man's land' in interstitial regions between spherical sites. To cross-check the analysis, we also deployed the unsupervised landmark algorithm recently developed by Kahle *et al.* [15]. Although automated, the algorithm does depend on a range of parameters which specify the spatial and statistical resolution that defines sites. We selected a midpoint as 1, occupancy minimum as 0.2, clustering threshold of 0.9 and an assignment threshold of 0.75 because, with these parameters, the algorithm automatically identified 72 *c* sites and 215 (out of the total 216) *b*-sites as hopping residence points. Moreover, the algorithm confirmed the c-sites were tetrahedrally coordinated (T-sites), whereas the b-sites were octahedrally coordinated (O-sites). The residence times extracted using Kahle's algorithm are shown in Table II for comparison, and the agreement between the two methods is good. This shows most transitions are O→T hops, or the inverse T→O hops (over 80 %). As the vast majority of hops involve T↔O transitions using the O-site intermediary site, this scheme is very similar to that proposed by Danilkin *et al*. [8], although that work did not identify the smaller fraction of T↔T hops (16%). In contrast, Voneshen *et al.*[3] argued that the T↔T hops are the main source of diffusion, but they did not identify the T↔O hops. Nevertheless, the mechanism in the AIMD is broadly consistent with the hopping mechanism known in other fluorite fast-ion conductors (CaF_2) [22, 25].

Table II: Theoretical residence times extracted from landmark analysis for the 700 K AIMD trajectory. The residence time is defined as average time in a site spent before a hop occurs, whereas the hop rate is the total number of hopping events per picosecond. Detailed balance requires the residence type in the 8c octahedral sites to be half that within the 4c tetrahedral sites owing to the multiplicity of the sites.

	The dominant hopping vector direction	Proportion events	Residence time – Spherical landmarks (ps)	Hop rate (ps^{-1})	Residence time – Voronoi landmarks (ps)
T↔T	[100]	16%	3.9	0.03	4
O→T	[111]	41%	2.0	0.11	1.6
T→O	[111]	41%	3.9	0.11	3.2
O→O	[110]	2%	>200 ps	0.005	N.A.

To visualize the hopping pathways, Fig. 4 (a) shows the copper density map calculated from the AIMD at 700 K. The density contains clear regions of high density at the tetrahedral positions and medium density at the octahedral positions. This results in a distinctive "Swiss-cheese" isosurface when viewed along the [001] projection caused by the lower density along <100> vectors associated with the rarer T↔T transitions. To pinpoint the hopping directions, the density was visualized on 2D slices along the (100) and (11-2) planes are shown in Fig. 4(b)-(d). Transitions between the copper sites appear as blurred intensity connecting two distinct sites. Clearly, there are very few transitions evident between the tetrahedral sites in Fig. 4(b). In contrast, there are clear transitions between T↔O sites in Fig. 4(c). Further inspection in Fig. 4(d), shows that many of these T↔O events occur along <111> directions, as expected according to the simple model in Section 3.1. Simulations were also run for a slightly non-stoichiometric $Cu_{2-x}Se$ cell with $Cu_{1.99}Se$, but the results were qualitatively identical, and are not presented for brevity, although the small shifts in the diffusion coefficient are included in Fig. 8.

In summary, all the available analysis shows that the short T↔O hops are the dominant diffusion pathway in Cu_2Se, and T↔T hops are far rarer. In a later section, we show that the quasielastic neutron scattering is consistent with this picture, after correction for complexities arising from the confined diffusion component and coherent acoustic phonons.

3.3 Experiment: Inelastic neutron scattering and X-ray diffraction

Past work has established that off-stoichiometry in $Cu_{2-x}Se$ can strongly affect the obtained diffusion coefficients and phase transition point [26]. To quantify the level of the off-stoichiometry and transition temperature, Fig. 5(a) shows the experimental X-ray diffraction maps which illustrate the phase transition point for Cu_2Se. The low angle (004) peak is a signature of the monoclinic phase. The integrated intensities of the (004) and ($\bar{3}31$) Bragg peaks are shown in Fig. 5(b). To determine the critical temperature, and the "apparent critical exponent", we have fitted the peak area of the (004) peak to the relationship, $A = \left(\frac{(T_c - T)}{T_c}\right)^{\beta}$ and obtained T_c= 395 ± 5 K, β=0.86 ± 0.1. The transition temperature indicates that our sample is stoichiometric to within 1-3% since the phase transition temperature varies as ($T_c = 405 - 2.5x$) [27, 28]. The Rietveld refinement in Fig. 5(c) confirms the expected site occupancies, and that Cu_2Se is in the Fm-3m space group, and the results are consistent with the reported structure (*#ICSD 54916).* We note that the literature is still divided on whether this is a first or second-order transition, and the uncharacteristically large β exponent suggests that this transition is not reliably described by critical theory. Instead, this phase transition is most likely of first-order but gives rise to "apparent critical phenomena" by virtue of its complex phase diagram [4]. In support of this, there is a smooth evolution of the DOS above, below and across the phase transition (Fig. 5(d)), and there is no strong evidence of soft-phonons. To examine the low energy range of the GDOS, an enlarged region is shown in Fig. 5(e).

Using the correlation functions obtained from the AIMD, it is possible to compare the vibrational density of states with the values measured in the inelastic neutron scattering. Fig. 5(d) compares the generalized density of states in the experiment with those calculated from AIMD. The agreement is almost perfect, indicating the AIMD simulations do an excellent job at capturing the main optical modes in Cu_2Se in the energy range 5 – 20 meV. This leads to excellent agreement with the experimental data over the entire temperature range because the GDOS is almost temperature-independent between 300 – 700 K (Fig. 5(d), see supplemental). Importantly, the phonon spectrum is similar at all temperatures, with two major peaks at 10 meV and 23 meV in both the low temperature data (300 K) and the superionic phase (T > 400 K). The similar overall intensities indicate that there is no major systematic loss of the transverse acoustic modes because, if that was the case, the number states/intensity would be reduced by two thirds. Close examination, however, does show that there are subtle changes in the phonon lifetimes in this temperature range which leads to minor broadening of some modes, particularly in the sub-THz regime (< 4meV) (Fig. 5(e)). The effects in this region, which are dominated by low energy acoustic phonons, are still relatively minor. Indeed, this is supported by the fact that the thermal conductivity above the phase transition temperature, far away from the transition, is only lowered by about 25% even at the hottest temperature (850 K) compared to the low-temperature phase (Fig. 5(f)), again supporting the notion that the phonon structure is very similar. The partial densities of states for the copper and selenium contributions in the superionic state are included in the supplementary materials, showing a large contribution of copper modes at low frequency.

To go beyond the angular-averaged DOS, Fig. 6(a) shows the measured neutron scattering function $S(\omega, Q)$ for Cu_2Se at 675 K, compared with the theoretical $S(\omega, Q)$ calculated from the AIMD decomposed into its coherent (Fig. 6(b)) and incoherent contributions (Fig. 6(c)), where the total measured $S(\omega, Q) = S_{coh}(\omega, Q)+ S_{inc}(\omega, Q)$. The coherent part of the neutron scattering function $S_{coh}(\omega,Q)$ involves the Fourier transform of time-correlation functions of pairs of different atoms' positions (e.g depending on $R_i(t)$ and $R_j(t)$ where R_x is a position operator for atom x, and i and j are indices for different atoms). The latter includes strong contributions from collective motions such as phonons. In contrast, the incoherent part of the $S_{inc}(\omega,Q)$ *is* generated by the self-correlation function of a single atom's time-dependent position (e.g depends on R_i and $R_i(t)$), and is an indication of self-diffusion. The latter generates a distinctive broadening of the elastic line near ω=0, known as the quasielastic contribution, which is a hallmark of diffusive processes. In both the experiment and incoherent theory for Cu_2Se, a strong quasielastic broadening is observed at the E=0 line for all *Q*-values which is an unambiguous indication that diffusion processes are taking place. The linewidth increases with Q as expected for long-range diffusion. But at high *Q* (~ 2.3 $Å^{-1}$), the experimental broadening suddenly increases, whereas the theoretical $S_{inc}(\omega, Q)$ does not.

The explanation for this can be seen by examining the theoretical pure coherent $S_{coh}(\omega, Q)$ which shows strong intensity at these Q-positions corresponding to acoustic phonons with a high dispersion that survives in the superionic state of Cu_2Se. The excellent qualitative and quantitative agreement with experiment gives us confidence in the other predictions of the AIMD, and next, we examine the low-energy realm in the quasielastic region below 1.2 THz (5 meV).

3.4 Experiment: Quasi-elastic neutron scattering

Quasielastic neutron scattering examines the energy region around the elastic line at $S(0+\delta, Q)$ (typically within a few meV in a time-of-flight experiment) and is a well-established technique to determine self-diffusion coefficients in materials, because it offers energy and reciprocal space vector (Q) resolution. The broadening of the elastic line via the quasielastic component can be analyzed to determine the self-diffusion of the ionic species including the length of the jumping vectors involved. QENS has the advantage over DC/AC transport measurements in that no sample contacts are needed, and it is free of geometric artifacts. The disadvantage of QENS is that it is an indirect method which relies on fitting to a model to determine the diffusion coefficient. Although there have been several attempts to measure the diffusion constant of Cu_2Se using both AC/DC transport and QENS, there is considerable disagreement in the reported diffusion coefficients [3, 8, 9, 11, 29]. The first reports by Takahashi *et al.* [29] obtained diffusion coefficients using DC transport that were two orders of magnitude smaller than obtained later using similar methods by Horvatić [11]. Subsequent QENS work by Danilkin *et. al.* found values broadly consistent with those of Horvatić (marginally higher) [8, 9]. However, recent QENS work by Voneshan *et. al.* [3] found values closer to those of Takahashi *et al.* [29]. The main difference between the work of Danilkin and Voneshan lies in the quite different models used to fit the QENS data. In this section we present a modified model that can place upper and lower bounds on the diffusion coefficient, and is generally applicable for superionic conductors. In particular we emphasize the coexistence of local "confined" diffusion for copper trapped in a site for long periods, together with sporadic jump events that lead to long-range copper migration. For brevity, the detail of our model and its validity is discussed in the supplemental materials and here we only present the main results.

After restricting the ω/Q range to avoid coherent (phonon-like) contributions (discussed in the supplemental materials), we then fit multiple Lorentzians which describe the confined diffusion and long-range diffusion components which are differentiated by their unique Q dependence of the energy-width. The minimal model that describes the low energy data at 675 K is a sharp elastic peak in combination with two distinct Lorentzian quasielastic peaks centered at zero energy:

$$S(Q,\omega) = A(Q)\delta(\omega) + \big(1 - A(Q)\big)L_1(\omega) + L_2(\omega, Q)$$

where δ is the Dirac delta function describing the elastic line, *A(Q)* is an the elastic incoherent structure factor, L_1 is a Lorentzian with a fixed Q-independent energy width, and L_2 is a Lorentzian with a Q-dependent width. This is convoluted to include the broadening caused by the instrumental resolution function measured using a vanadium standard. In the supplemental materials, it shown that both L_1 and L_2 are required to fit the data. As detailed in the supplemental, the first Lorentzian captures the effect of confined diffusion where the Cu is trapped for long periods in a local region of the lattice. The second Lorentzian describes long range diffusion where the Cu moves between adjacent regions in the lattice. Using this model, and accounting for the instrument resolution effects, Figure 7 shows that the QENS spectra are very well fitted. Figure 7(b) shows the Q dependency of the data and model. The confined diffusion is tied to high-frequency vibrations thus giving a broader energy width for L_1, with a full-width-half-maximum of $\Gamma_1 = 3.5\pm0.5$ meV that is independent of Q. The long-range diffusion described by L_2 leads to a narrower E-width (Γ_D) that is Q-dependent and increases as Q^2, at low momentum transfer shown in Fig 7(c), which is a signature of long range diffusion . It is physically reasonable that Γ_D is an order of magnitude smaller than Γ_1 because an ion will experience many unsuccessful trial vibrations orbiting an average position before finally transitioning to a new crystallographic site, and this is reflected in the lower frequency-width of Γ_D.

Having extracted the key parameter related to long-range diffusion, namely Γ_D, we employ the Chudley Elliot (CE) model to relate the Q-dependence to the diffusion coefficient [30], where the FWHM from the diffusive component is:

$$\Gamma_D = \frac{2\hbar}{\tau}\left(1 - \frac{\sin(Qd)}{Qd}\right) \tag{2}$$

where τ is the hopping time, and d is the hopping length and the diffusion coefficient is $d^2/6\tau$. This model was selected because it correctly captures the trends in the Q-dependence (see supplemental materials), and allows us to compare hopping times extracted from the *ab-initio* molecular dynamics. A common approach would be to fit the CE model to Fig. 7(c), shown by the dotted line, where the fits give a d = 2.79 ± 0.19 Å, τ =1.86 ± 0.06 ps. This value of d is intermediate between the values expected for O↔T and T↔T (2Å and 3Å). However, one can note that not all points in Fig. 7(c) are equally well described by the line of best fit. The single-component CE model assumes that all hops occur with a unique jump length, whereas if there is a distribution this could be an oversimplification. If the distribution is sufficiently bimodal to correspond to distinct O↔T and T↔T hops, one would expect an additional Lorentzian (L_3) would be observed experimentally. The fact that this Lorentzian is not observed in practice indicates both types of hop have a similar FWHM making them indistinguishable within experimental resolution – a scenario that is shown to be likely in Fig. S5. Thus, to place bounds on the Cu_2Se data we adopted a different strategy detailed in the supplemental materials. Essentially, we insist that all Γ_D experimental points need to be encapsulated within the shaded regions in Fig. 7(c) determined by using d = 2 Å or 3 Å for T↔O or T↔T hops, and upper and lower estimates for τ. The resulting limits for the bounding choices on the CE model are shown in Table III, giving diffusion coefficients bounded from 1.9 - 4.2 (× 10^{-5} $cm^2.s^{-1}$) with an average of 3.1 × 10^{-5} $cm^2\cdot s$ bounded in the range of +- of 1.3 × 10^{-5} $cm^2\cdot s$ which agrees well with the *ab-initio* simulations.

Table III: Bounded diffusion coefficients obtained at 675 K for different Chudley-Elliot models.

Model	d (Å)	τ (ps)	D ($\times 10^{-5}$ $cm^2.s^{-1}$)
T↔T upper limit	3	3.6	4.2
T↔T lower limit	3	4.8	3
T↔O upper limit	2	2.5	3.3
T↔O lower limit	2	4	1.9
Simple best fit	2.79 ± 0.19	3.72 ± 0.12	3.4

3.5 Comparison of diffusion coefficients between AIMD and experiments

Using the approach described above, Figure 8 compares the diffusion coefficients obtained from AIMD, QENS and transport experiments together with past reports. The Nernst equation was used to convert the measured conductivities in the transport experiments to a diffusion coefficient. The results reported here from AIMD and QENS line up well with the transport experiments of Horvatić *et al.* [10, 11] and fall within the green band in the figure. Overall, the new values are only a little smaller than those determined by Danilkin *et al.* [8] but are almost 10^2 times greater than those reported by Voneshen *et al.* [3] and the transport measurements of Takahashi *et al.* [29]. We consider the convergence between our AIMD, our QENS work and that of Horvatić and Danilkin to be satisfactory [31]. It remains unclear why our results differ from Ref [3] and [29], however, our study has given all of the details of our fitting procedure, explained the uncertainties clearly and compared closely with theoretical calculations for the first time, and we are thus confident in our results. We also note that Ref [3] contains an error in the expression for the random walk diffusion coefficient described in the supplementary material which has the incorrect dimensions. Meanwhile, Horvatić *et al.* earlier argued [10, 11] that geometric factors introduced artifacts into Takahashi *et al.*'s [29] earliest transport measurements. The lack of any sudden increment in the diffusion coefficient in Takahashi *et al.*'s measurements at the monoclinic-cubic transition is also at odds with nearly every other measurement for Cu_2Se, and it is therefore reasonable to query the data above the transition.

Despite the quantitative differences in the absolute diffusion coefficient, there are also similarities between all of the datasets in that they appear to follow a similar Arrhenius law above 400 K such that:

$$D(T) = D_0 e^{-E_A/(k_b T)} \tag{7}$$

with a similar activation energy E_A in the range of 90 – 210 meV (albeit with very different values of D_0). The range of activation energies also agrees with the energies determined electrochemically under isothermal conditions [29] and the AIMD. For example, from the *ab-initio* molecular dynamics, E_A is 210 meV and D_0 is 6.124×10^{-4} cm^2/s. The barrier derived from the neutron and Horvatić's work is 90 meV. These values are also in reasonable agreement with the barriers expected for the T→O hop calculated using the nudged-elastic band method described in Section 3.1

4. Conclusions

Using a combination of simulations and experiments, we have provided a new determination of the diffusion coefficients and pathways for copper motion in Cu_2Se. Careful treatment of the QENS data leads to a value that is in reasonable agreement with the *ab-initio* theory and Horvatić *et al*.'s transport measurements. These insights are essential to understand the analogous effects in more complex nanocomposite forms of Cu_2Se [18]. So, what are the implications for thermal transport in Cu_2Se more generally? It is well established that the contribution of ionic diffusion to the thermal conductivity is negligible compared to the heat transport by phonons. Nevertheless, the standard paradigm is that Cu diffusion does indirectly affect the phonon transmission by introducing scattering or removing certain phonon modes. Contrary to this assumption, the direct experimental evidence shows an almost temperature-independent phonon DOS in our work, as in past work [3], in the window where superionic motion is speeding up by orders of magnitude. Although the hopping rates do increase exponentially, the hopping timescales are well below the speed limit of the THz phonons which constitute most of the phonon modes in Cu_2Se residing above 10 meV, as originally pointed out by Voneshen et al. [3]. It was proposed that for ionic motion to have a maximal effect on the phonons, the copper hopping rates should be on the same or faster timescale than the heat-bearing phonons. In Cu_2Se, the ionic diffusion does not break the critical speed limit to affect the majority of the phonons. Since copper diffusion is not the main factor determining the low thermal conductivity, we propose that it would be worthwhile to explore chemical approaches which suppress the fast-ionic diffusion. This could potentially solve an important issue because the long-range mobility of the Cu ion in Cu_2Se poses a major technological barrier for real-world applications because prolonged exposure to strong electric fields leads to undesired electromigration and device degradation [19].

As a more subtle point, we have also identified an alternate mechanism for phonon scattering: the dynamic creation and destruction of Frenkel defects. The role of this mechanism on the sub-THz phonons needs to be clarified although the overall effect on thermal conductivity must be rather subtle as the conductivity only varies by 25% between 300 K and 850 K, even as the defect-creation rates (equal to the T-O hopping rates) change by orders of magnitude. Importantly, the dynamic generation of Frenkel defects does not necessarily require long-range copper diffusion, as it is essentially a local motion. In the future, it could be beneficial to adjust the structure-function relationship in new crystal phases derived from Cu_2Se to suppress the long-range diffusion whilst maximizing phonon-scattering.

Acknowledgements

We thank ANSTO for providing access to PELICAN at the Australian Centre for Neutron Scattering and to the Powder Diffraction beamline at the Australian Synchrotron. High performance computation was performed on the RAIJIN and PAWSEY supercomputers within the National Computer Infrastructure.

Conflict of Interest

The authors declare no conflict of interest.

References:

[1] H. Liu, X. Shi, F. Xu, L. Zhang, W. Zhang, L. Chen, Q. Li, C. Uher, T. Day, G.J. Snyder, Copper ion liquid-like thermoelectrics, Nature Materials 11(5) (2012) 422-425.
[2] M. Li, D.L. Cortie, J. Liu, D. Yu, S.M.K.N. Islam, L. Zhao, D.R. Mitchell, R.A. Mole, M.B. Cortie, S. Dou, Ultra-high thermoelectric performance in graphene incorporated Cu_2Se: Role of mismatching phonon modes, Nano Energy 53 (2018) 993-1002.
[3] D.J. Voneshen, H.C. Walker, K. Refson, J.P. Goff, Hopping Time Scales and the Phonon-Liquid Electron-Crystal Picture in Thermoelectric Copper Selenide, Phys. Rev. Lett. 118(14) (2017) 145901.
[4] S.D. Kang, S.A. Danilkin, U. Aydemir, M. Avdeev, A. Studer, G.J. Snyder, Apparent critical phenomena in the superionic phase transition of $Cu_{2-x}Se$, New J. Phys. 18 (2016) 013024.
[5] B. Li, H. Wang, Y. Kawakita, Q. Zhang, M. Feygenson, H.L. Yu, D. Wu, K. Ohara, T. Kikuchi, K. Shibata, T. Yamada, X.K. Ning, Y. Chen, J.Q. He, D. Vaknin, R.Q. Wu, K. Nakajima, M.G. Kanatzidis, Liquid-like thermal conduction in intercalated layered crystalline solids, Nature Materials 17(3) (2018) 226-230.
[6] J.L. Niedziela, D. Bansal, A.F. May, J. Ding, T. Lanigan-Atkins, G. Ehlers, D.L. Abernathy, A. Said, O. Delaire, Selective breakdown of phonon quasiparticles across superionic transition in $CuCrSe_2$, Nature Physics 15(1) (2019) 73-78.
[7] L.P. Bulat, D.A. Pshenay-Severin, A.A. Ivanov, V.B. Osvenskii, Y.N. Parkhomenko, On the Heat Capacity of Cu2Se, Journal of Electronic Materials 46(5) (2017) 2778-2781.
[8] S.A. Danilkin, M. Avdeev, M. Sale, T. Sakuma, Neutron scattering study of ionic diffusion in Cu–Se superionic compounds, Solid State Ionics 225 (2012) 190-193.
[9] S.A. Danilkin, M. Avdeev, T. Sakuma, R. Macquart, C.D. Ling, M. Rusina, Z. Izaola, Neutron scattering study of short-range correlations and ionic diffusion in copper selenide, Ionics 17(1) (2011) 75-80.
[10] M. Horvatić, Z. Vučić, DC ionic conductivity measurements on the mixed conductor $Cu_{2-x}Se$, Solid State Ionics 13(2) (1984) 117-125.
[11] M. Horvatić, I. Aviani, M. Ilić, Two-point dc ionic conductivity measurements in the superionic phase of $Cu_{2-x}Se$, Solid State Ionics 34(1) (1989) 21-24.
[12] G. Kresse, J. Furthmüller, Efficient iterative schemes for ab initio total-energy calculations using a plane-wave basis set, Physical Review B 54(16) (1996) 11169-11186.
[13] G. Kresse, J. Furthmüller, Efficiency of ab-initio total energy calculations for metals and semiconductors using a plane-wave basis set, Computational Materials Science 6(1) (1996) 15-50.
[14] G. Kresse, Ab initio molecular dynamics for liquid metals, Journal of Non-Crystalline Solids 192-193 (1995) 222-229.
[15] L. Kahle, A. Musaelian, N. Marzari, B. Kozinsky, Unsupervised landmark analysis for jump detection in molecular dynamics simulations, Physical Review Materials 3(5) (2019) 055404.
[16] K. Momma, F. Izumi, VESTA 3 for three-dimensional visualization of crystal, volumetric and morphology data, Journal of Applied Crystallography 44(6) (2011) 1272-1276.
[17] W. Humphrey, A. Dalke, K. Schulten, VMD: visual molecular dynamics, Journal of Molecular Graphics 14(1) (1996) 33-38.
[18] G.R. Kneller, V. Keiner, M. Kneller, M. Schiller, nMOLDYN: a program package for a neutron scattering oriented analysis of molecular dynamics simulations, Computer Physics communications 91(1-3) (1995) 191-214.

[19] T. Róg, K. Murzyn, K. Hinsen, G.R. Kneller, nMoldyn: a program package for a neutron scattering oriented analysis of molecular dynamics simulations, Journal of Computational Chemistry 24(5) (2003) 657-667.
[20] K. Hinsen, E. Pellegrini, S. Stachura, G.R. Kneller, nMoldyn 3: Using task farming for a parallel spectroscopy-oriented analysis of molecular dynamics simulations, Journal of Computational Chemistry 33(25) (2012) 2043-2048.
[21] D. Yu, R. Mole, T. Noakes, S. Kennedy, R. Robinson, Pelican — a Time of Flight Cold Neutron Polarization Analysis Spectrometer at OPAL, Journal of the Physical Society of Japan 82(Suppl.A) (2013) SA027.
[22] N.T. Wilson, M. Wilson, P.A. Madden, N.C. Pyper, Interionic interactions and fast ‐ ion conduction in CaF2, J. Phys. Chem. Phys. 105(24) (1996) 11209-11219.
[23] H. Kim, S. Ballikaya, H. Chi, J.-P. Ahn, K. Ahn, C. Uher, M. Kaviany, Ultralow thermal conductivity of β-Cu_2Se by atomic fluidity and structure distortion, Acta Materialia 86 (2015) 247-253.
[24] A.K. Sagotra, D. Chu, C. Cazorla, Influence of lattice dynamics on lithium-ion conductivity: A first-principles study, Physical Review Materials 3(3) (2019) 035405.
[25] M.J. Gillan, Collective dynamics in super-ionic CaF_2. II. Defect interpretation, Journal of Physics C: Solid State Physics 19(19) (1986) 3517-3533.
[26] A.N. Skomorokhov, D.M. Trots, M. Knapp, N.N. Bickulova, H. Fuess, Structural behaviour of β-$Cu_{2-\delta}Se$ (δ=0, 0.15, 0.25) in dependence on temperature studied by synchrotron powder diffraction, Journal of Alloys and Compounds 421(1) (2006) 64-71.
[27] D.J. Chakrabarti, D.E. Laughlin, The Cu−Se (Copper-Selenium) system, Bulletin of Alloy Phase Diagrams 2(3) (1981) 305-315.
[28] R.D. Heyding, The copper/selenium system, Canadian Journal of Chemistry 44(10) (1966) 1233-1236.
[29] T. Takahashi, O. Yamamoto, F. Matsuyama, Y. Noda, Ionic conductivity and coulometric titration of copper selenide, Journal of Solid State Chemistry 16(1) (1976) 35-39.
[30] C. Chudley, R. Elliott, Neutron scattering from a liquid on a jump diffusion model, Proceedings of the Physical Society 77(2) (1961) 353.
[31] F. Volino, A.J. Dianoux, Neutron incoherent scattering law for diffusion in a potential of spherical symmetry: general formalism and application to diffusion inside a sphere, Molecular Physics 41(2) (1980) 271-279.

Figures and Captions

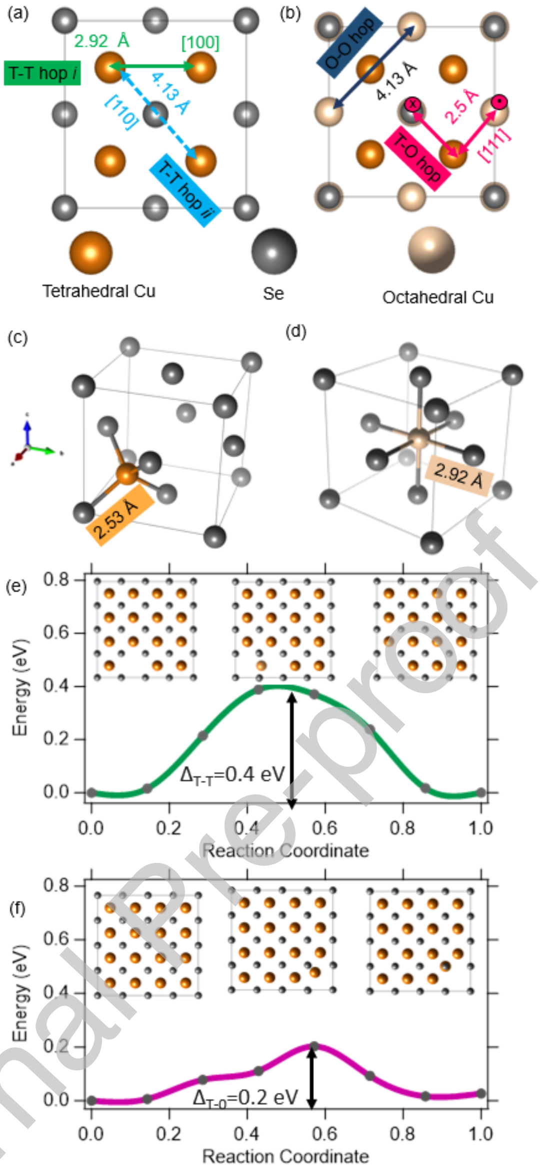

Fig. 1. (a) The time-averaged crystal structure of cubic Cu_2Se consists of a FCC selenium lattice, with copper primarily located in the tetrahedral positions. Hopping between nearest-neighbour Cu positions corresponds to [100] vectors. (b) The lightly occupied octahedral sites in the lattice provide another potential hopping route along the [111] directions, with a shorter hopping length. Note that [111] vectors contains out of-plane components. While the distances are given assuming idealized positions in the antifluorite structure, there can be considerable variation (±0.4 Å) if the non-idealised positions are used. (c) Illustration of the copper in the tetrahedral (b-site) position. (d) Illustration of copper at the octahedral O-site (c-Wyckoff position). (e) Energy profile calculated via DFT for copper undergoing a T-T hop. (f) Energy profile calculated via DFT for copper undergoing a T-O hop. The inset figures show the pathway taken by the copper atom.

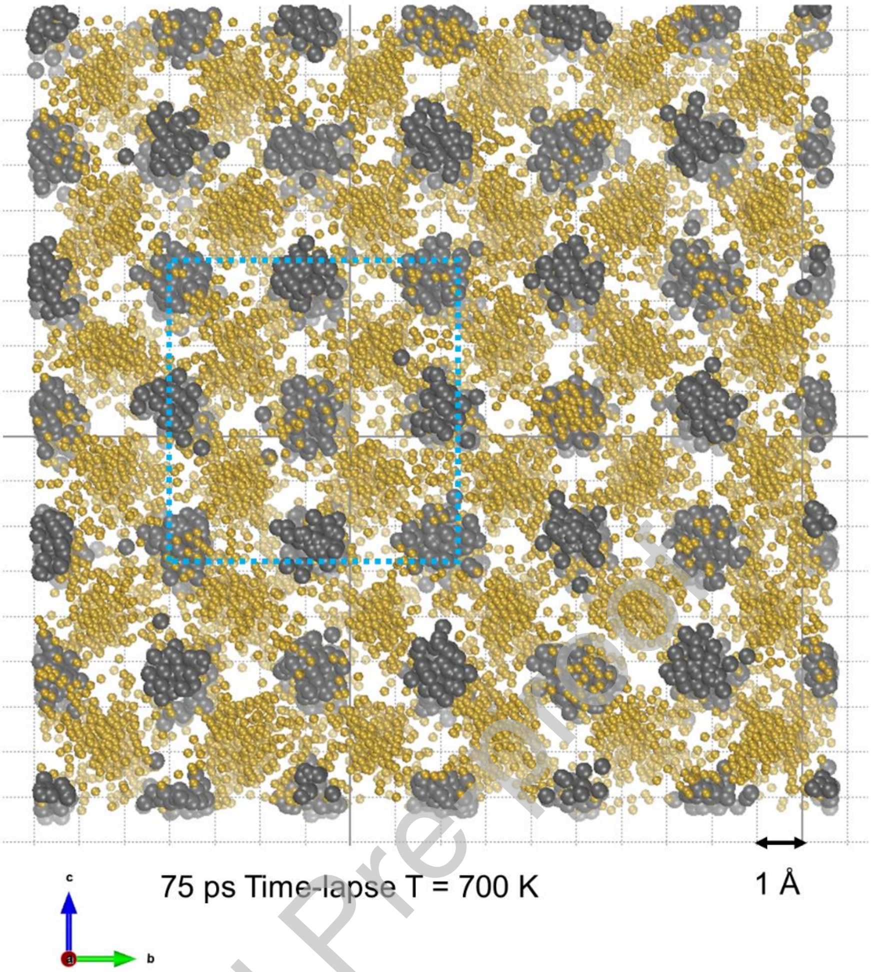

Fig. 2. Time-lapse image showing that the selenium atoms form a thermally agitated FCC lattice, whereas the copper atoms are delocalized across the crystal structure, albeit with a high probability of being located at the tetrahedral sites of the cubic lattice. The image is constructed using the trajectories from the 700 K *ab-initio* molecular dynamics with each still image taken 150 fs apart, and then superimposed on each other.

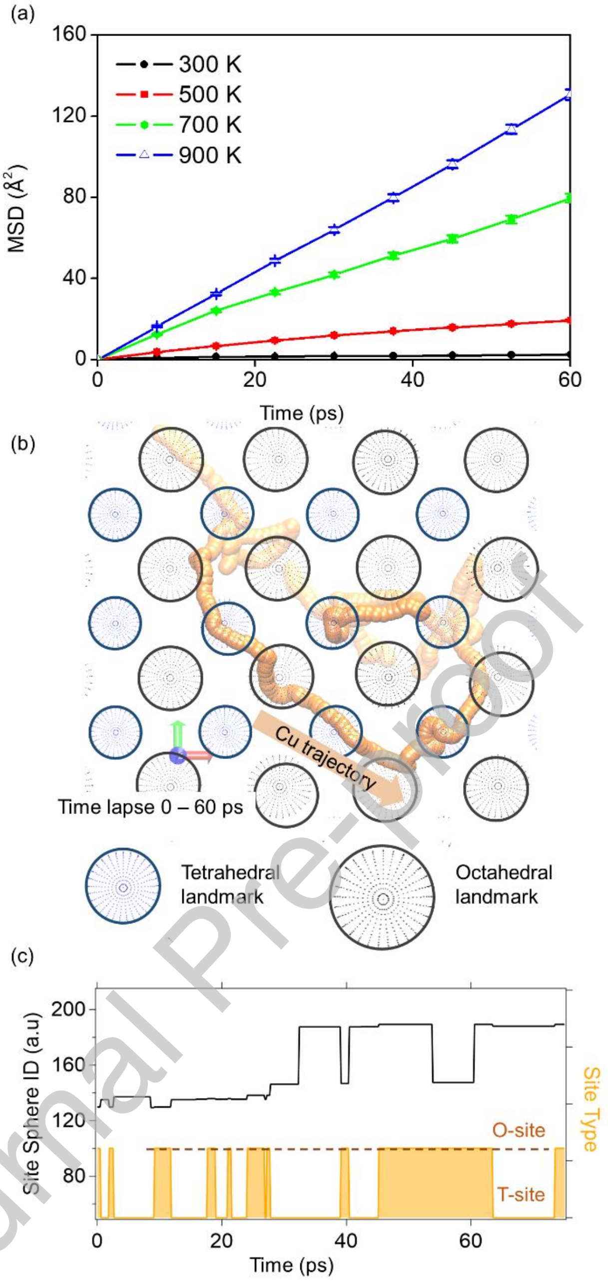

Fig. 3. (a) The mean-squared displacements calculated from the AIMD trajectories at various temperatures. (b) A time-lapse image of the motion of a single copper atom shows the hopping motion of the ion as it navigates through the T-site and O-site landmarks. The time-lapse is from the 700 K trajectory over a period of 60 ps with each frame visualized 100 fs apart. The brightness of the copper indicates its height in z, into or out of the page. (c) Landmark analysis showing residence periods for a copper ion as it moves between tetrahedral and octahedral landmark sites during the trajectory.

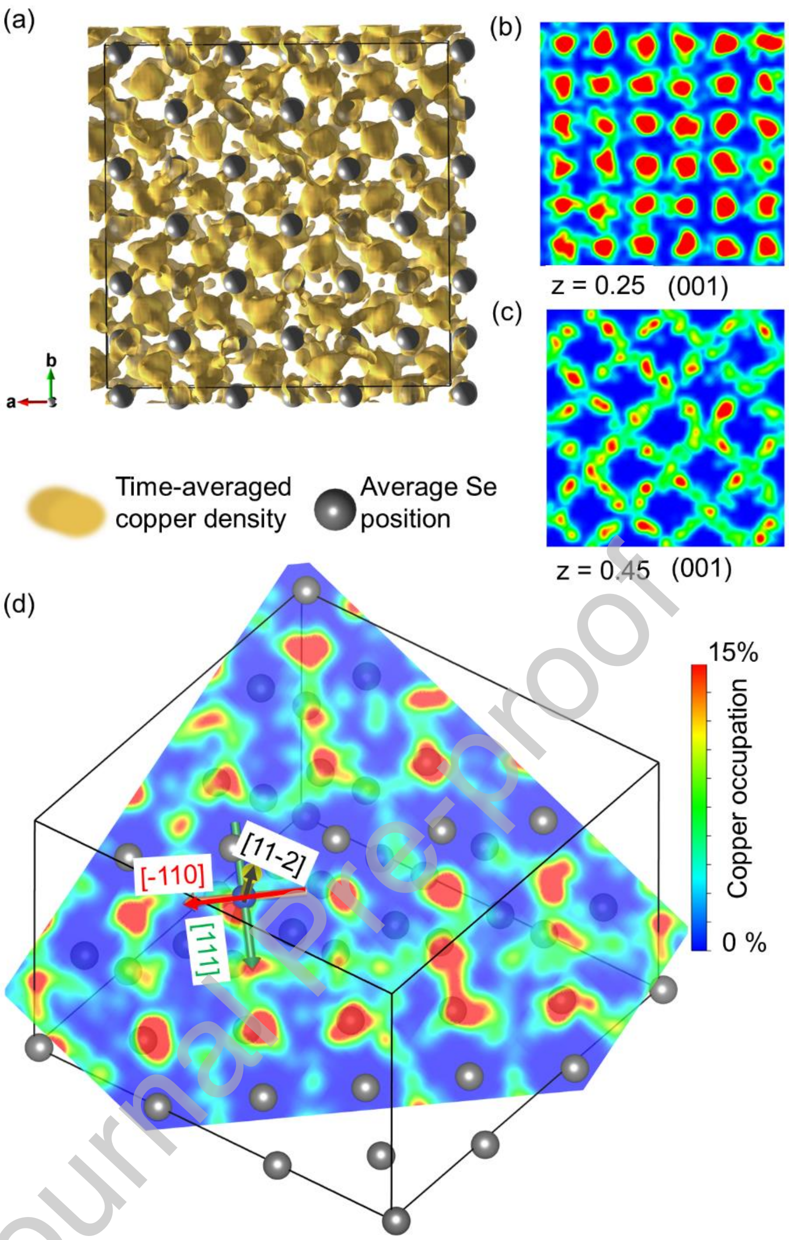

Fig. 4. (a) The copper density map from AIMD is visualized as an isosurface connecting regions where the copper occupation is greater than 5%. (b) A 2D slice of density map on a plane normal to (001) shows the heavily occupied tetrahedral sites at the z = -0.25 positions which are generally disconnected from one another indicating low probability of direct T↔T transitions. (c) The (001) slice at z = 0.45 shows the transition pathways between the T-sites and O-sites, which appear to be along the [110] directions. (d) A isometric view of the [11-2] slice superimposed on the crystal structure shows the main transition pathways between the T↔O transitions for hopping vectors in the plane along the [111] directions.

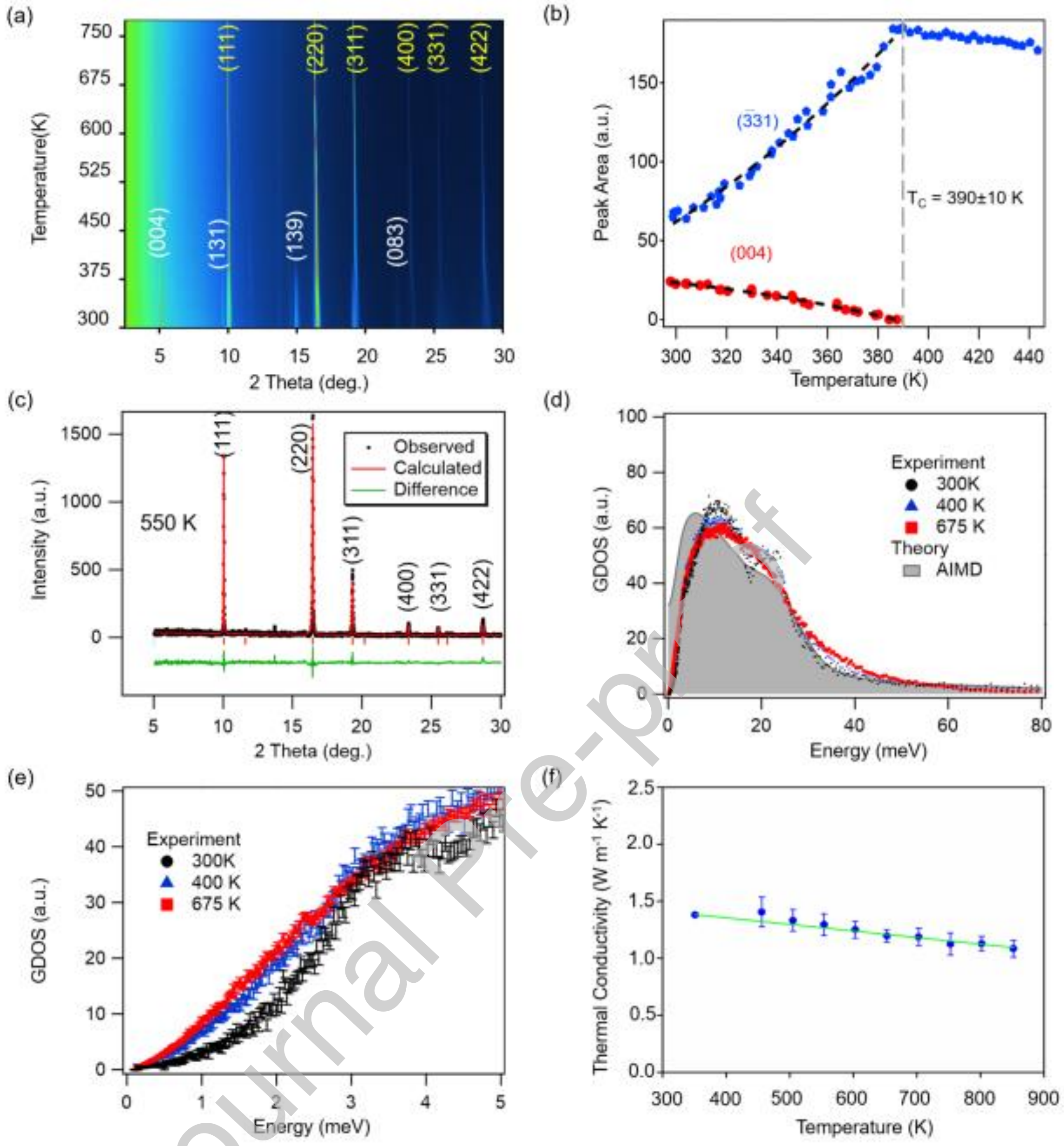

Fig. 5. a) X-ray diffraction patterns for a temperature-sequence stacked in a heatmap. The (004), (131), (139) and (083) reflections are associated with the low temperature phase of Cu_2Se. b) Integrated peak intensity for the (004) and ($\bar{3}$31) monoclinic peaks from the XRD c.) Rietveld refinement of the XRD data at 550 K. d) Experimental generalised density of states in Cu_2Se at 300, 400, and 675 K, compared with the theoretical DOS calculated from the AIMD at 675 K. e) Enlargement of the low-energy region of the DOS showing subtle changes in the acoustic phonon spectrum above and below the superionic transition. f) The thermal conductivity of Cu_2Se has an anomally (not shown) at the 400 K transition temperature, but overall is only weakly temperature-dependent.

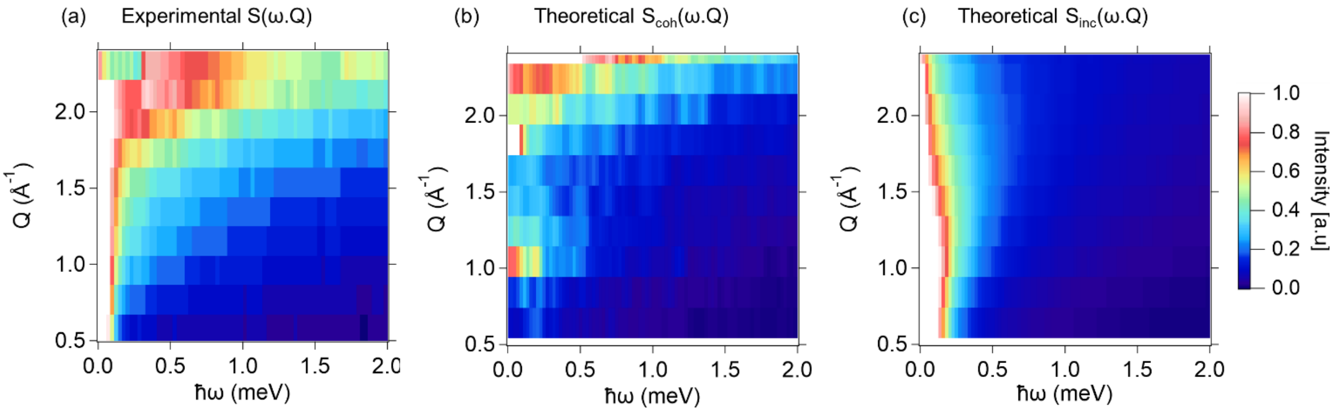

Fig. 6. (a) The total measured experimental $S_{tot} = S_{coh} + S_{inc}$ for Cu_2Se at 675 K. (b) The calculated S_{coh} from the AIMD simulations including low energy phonons. (c) The calculated S_{inc} from the AIMD simulations which depends on Cu self-diffusion

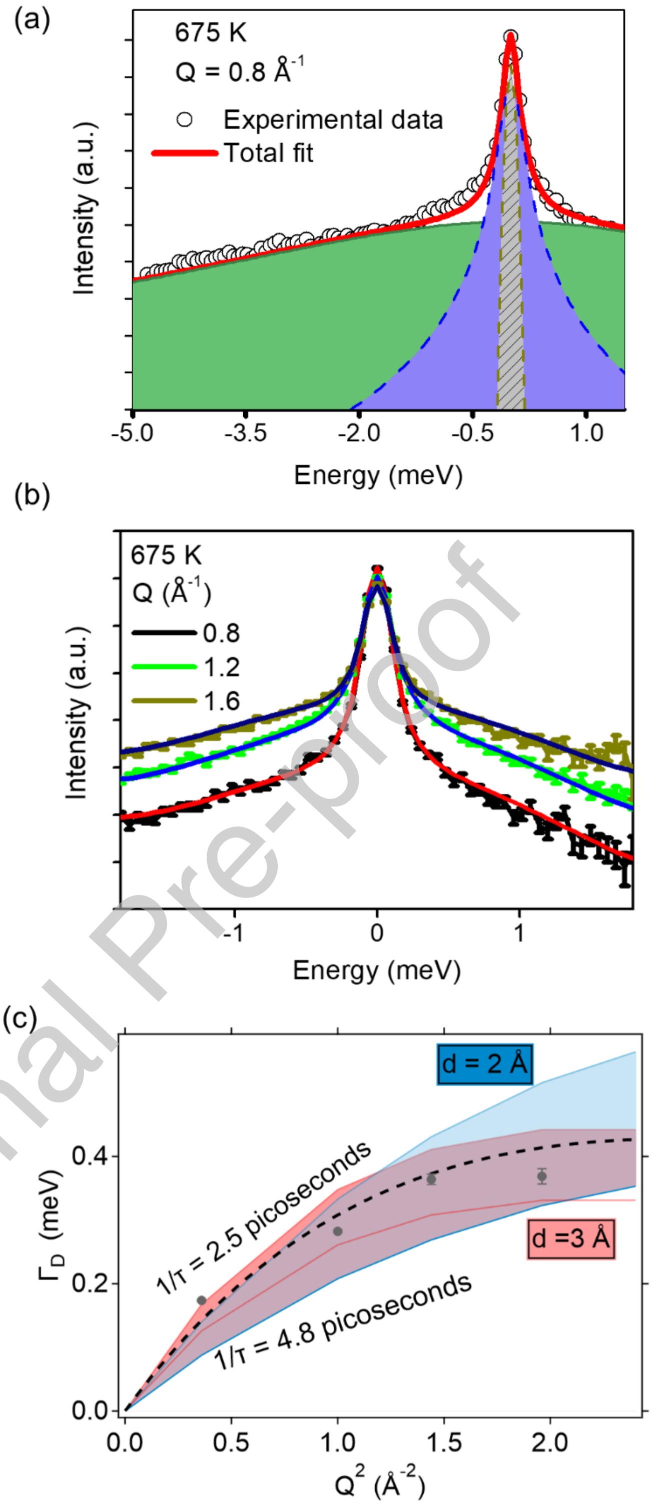

processes.

Fig. 7. (a) The low-Q quasielastic neutron spectra and fitting for Cu_2Se at 675 K. (b) Comparison of several Q values at 675 K. (c) Extracted FWHM for the narrower QENS components as a function of Q^2 at 675 K. The points are the experimental data. The dotted line is the line-of-best fit for D = 2.79 Å. The two shaded regions shows the limiting behavior

for 2 Å and 3 Å hops, which is the bounded range where statistically valid fits can be achieved.

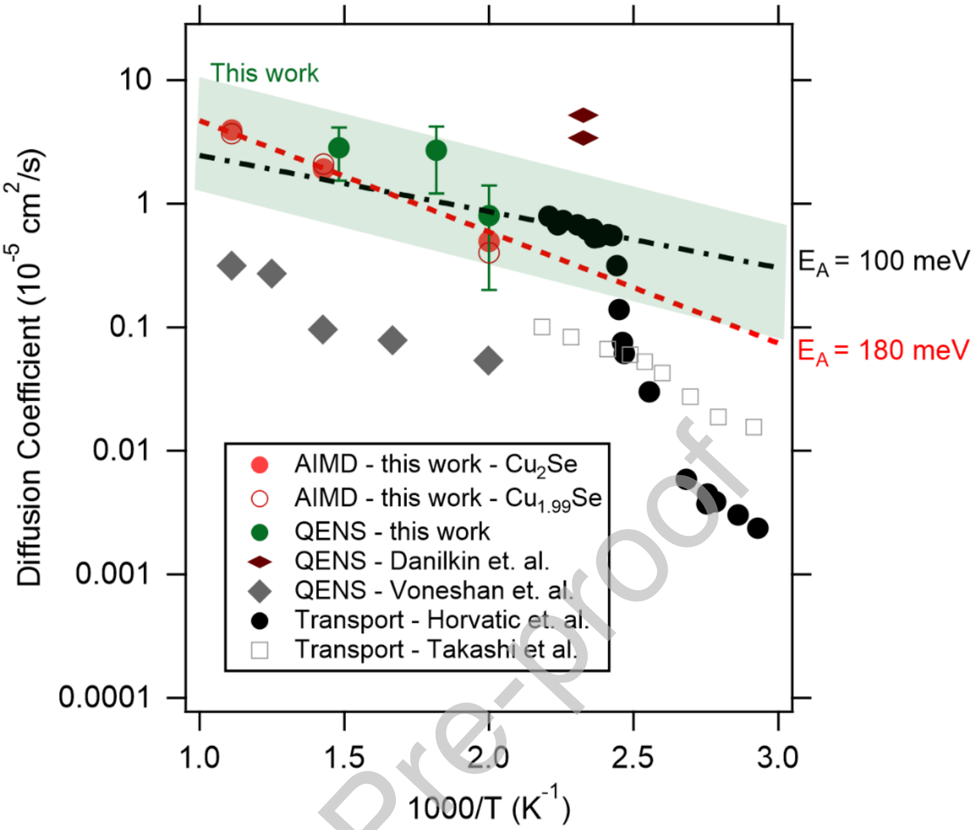

Fig. 8. Diffusion coefficients obtained in this work (encapsulated within the green bar), compared with past reports from both QENS and transport experiments.

Conflict of Interest

The authors declare that there are no conflicts of interest.

Acknowledgements

We acknowledge the support of ANSTO, in providing the access to PELICAN for this work. This research was undertaken, in part, using the Powder Diffraction beamline at the Australian Synchrotron. High performance computation was performed on the RAIJIN and PAWSEY supercomputers within the National Computer Infrastructure.

GraphicalAbstract

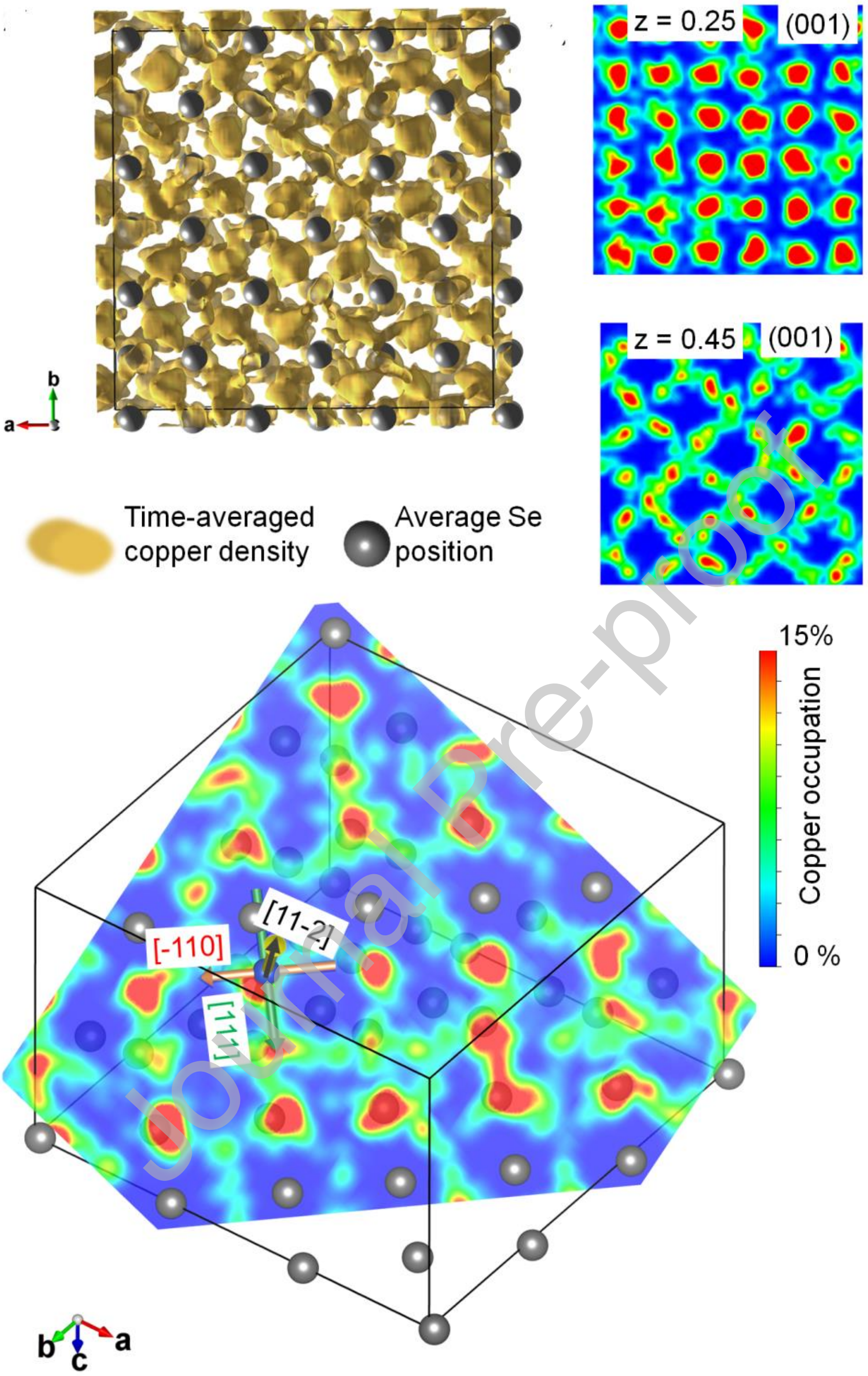

Supplementary materials

Copper Diffusion Rates and Hopping Pathways in Superionic Cu_2Se

Sheik Md Kazi Nazrul Islam[1, 2], Prince Mayank[3], Yulou Ouyang[4], Jie Chen[4], Arun. K. Sagotra[5], Meng Li[1], Michael B. Cortie[2], Richard Mole[6], Claudio Cazorla[5], Dehong Yu[6], Xiaolin Wang[1], Robert A. Robinson[1], David Laurence Cortie[*1]

[1] *The Institute for Superconducting and Electronic Materials, Australian Institute for Innovative Materials, University of Wollongong, North Wollongong, NSW 2500, Australia*

[2] *School of Mathematical and Physical Sciences, University of Technology Sydney, Broadway, NSW 2007, Australia*

[3] *Indian Institute of Technology Delhi, New Delhi 110016, India*

[4] *Center for Phononics and Thermal Energy Science, China-EU Joint Lab for Nanophononics, School of Physics Science and Engineering, Tongji University, Shanghai 200092, China*

[5] *School of Materials Science and Engineering, University of New South Wales, Sydney, 2052, Australia*

[6] *The Australian Nuclear Science and Technology Organisation, Lucas Heights, NSW 2232, Australia*

CORRESPONDING AUTHOR INFORMATION

Email address: dcortie@uow.edu.au (D. L. Cortie)

SI1. Technical Details of the DFT *ab-initio* Molecular Dynamics

The temperature in the AIMD simulations was kept fluctuating around a set-point value by using a Nose-Hoover thermostat. Supercells of 3x3x2 Cu_2Se unit cells, containing 216 atoms were used with periodic boundary conditions. Calculations were performed on the RAIJIN supercomputer which is part of the Australian National Computer Infrastructure. Newton's equations of motion were integrated using Verlet's algorithm and a time-step length of 1.5 femtoseconds (fs). Γ-point sampling for integration within the first Brillouin zone was employed. The simulations were equilibrated using 5 ps of run-time, and the total duration of each AIMD production run was for 120 ps.

SI2. Technical Details of the DFT Nudged Elastic Band Calculations

Our NEB calculations were performed for large 2x2x2 supercells containing 96 atoms. We used a dense q-point grid of 8x8x8 for first Brillouin zone sampling and an energy plane-wave cut-off of 650 eV.

SI3. Landmark Analysis of *ab-initio* Molecular Dynamics

Here we provide a very brief introduction to the concept of landmark analysis for any unfamiliar readers. In the standard approach of molecular dynamics, the atomic positions are written in Cartesian coordinates. While this is straightforward to visualize, it can make certain types of analysis difficult. For example, to analyze ionic hopping or chemical transport, it is desirable to identify when a chemical species has jumped from Site A to Site B. While, in principle, this can be extracted from the derivatives of the Cartesian positions, or by applying spatial thresholds, in practice this is complicated by the noise in the trajectory. Thus, it is generally advantageous to define new variables which depend only on the proximity to predefined landmark positions (e.g. a specific atom, a Voronoi center, a Wyckoff site) and use this to discriminate when jumping events have occurred. To identify the main hopping pathways in the Cu_2Se, we first performed an elementary type of landmark analysis by positioning landmarks at every tetrahedral and octahedral interstitial site (labelled as T-sites and O-sites from this point forward). During the trajectory, any Cu that strays within 1 Å of a landmark is tagged with a site ID number and the site type (O or T) belonging to the nearest landmark. If the Cu's site ID number changes, this corresponds to a hopping event, and by tracking the site types it possible to calculate the transition rates for O↔T, O↔O and T↔T transitions. In this way, hopping events and residence times, as well as transition probabilities can be identified. This was implemented using custom-written code in the Visualizing Molecular Dynamics (VMD) software. While the latter approach has the advantage of being simple, it does assume that landmarks can be defined as non-overlapping spheres positioned judiciously using prior knowledge of the crystal structure. Less biased landmark analysis can also be implemented using more sophisticated mathematics, by performing a decomposition of the Cartesian vectors into a new (non-orthogonal) basis set made of landmark vectors. If the landmark vectors are automatically positioned using Voronoi tessellation, similar landmark vectors can then be clustered automatically to identify special sites based on statistical criteria, and the resulting “site” can have an arbitrary shape. To this end, we also deployed the new SITATOR toolkit developed by Kahle *et al.* for “unsupervised” Voronoi landmark analysis.

SI4. Partial density of states from the *ab-initio* Molecular Dynamics

Figure S1 shows the vibrational density of states obtained from *ab-initio* molecular dynamics at 700 K, decomposed into Cu and Se contributions. Figure S2 shows the variation of the total density of states with temperature which shows only a subtle variation.

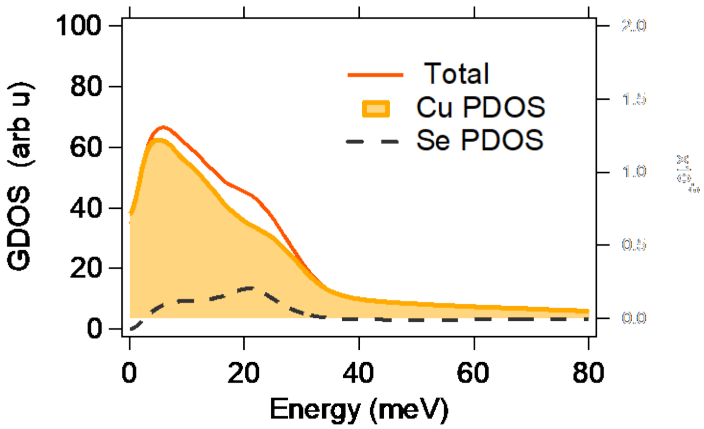

Figure S1. Partial density of states of the *ab-initio* molecular dynamics at 700 K

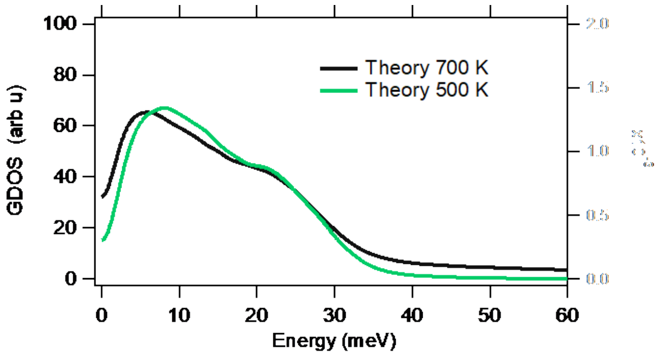

Figure S2. Temperature dependence of the DOS extracted from the *ab-initio* molecular dynamics

SI5. Geometric and Statistical Considerations for Diffusion in the Ideal Fluorite Crystal Structure.

Ideal Cu_2Se crystallizes in the anti-fluorite cubic structure, with the Se ions on a standard face-centered cubic (FCC) Bravais lattice, with lattice constant a. Within this lattice, there are two interstitial sites, a tetrahedral (T) interstitial site at (¼, ¼, ¼), (¼, ¼, ¾) plus FCC translational vectors, and a larger octahedral (O) interstitial site at (½, ½, ½) plus FCC translational vectors. The tetrahedral positions, if fully filled, form a simple-cubic lattice, with lattice constant a/2, and they satisfy the 2:1 stoichiometry of ideal Cu_2Se. In contrast, the octahedral positions would support a 1:1 stoichiometry. Cu_2Se is often thought of as a rigid selenium FCC lattice, with relatively mobile Cu ions on the tetrahedral interstitial sites.

The sizes of these interstitial sites, and the Cu-Se bond lengths, assuming that the copper ion would sit at the center of each respective polyhedron, are as listed in Table S1. The octahedral site is clearly larger than the tetrahedral site, but we know from the crystal structure that this is energetically unfavorable and in practice the T-site is the site where the majority of the Cu resides.

Table S1. The size of copper sites, and Cu-Se bond-length for the T and O sites in the cubic phase of Cu_2Se.

Interstitial/Vacancy site in ideal FCC lattice	Distance from centre of polyhedron to corners, i.e. Cu-Se bond distance	Number of (triangular) faces	Number of edges	Number of vertices
Tetrahedral at (¼, ¼, ¼) and (¼, ¼, ¾)	$\sqrt{3}$ a /4 = 0.433 a	4	6	4
Octahedral at (½, ½, ½)	a / 2 = 0.5 a	8	12	6

The FCC lattice can be considered as a network of edge-connected tetrahedra, or equivalently as a network of edge-connected octahedra, Table S2. If a Cu-ion is sitting within a tetrahedron, the most obvious way for it to leave its site is though one of the triangular faces, to one of the four neighboring octahedra (ideally along a [111] direction). It can also move directly from its tetrahedron to one of the 6 edge-connected tetrahedra, passing through the mid-point of one of the edges. This would involve hopping along a [100]-type direction. But these very same edges connect the octahedra to other octahedra (in a direction perpendicular to the direct T-T hop). In other words, the direct O-O hop would take place along [110]-type directions. Hopping through a vertex, would involve a head-on collision with the selenium lattice points, and is therefore very unlikely. In other words, the most open channels in the structure are through the polyhedron faces along [111]-type directions, from T→O or O→T. Less likely are the direct T→T [100]-type or O→O [110]-type hops, though the polyhedron edges. The next-nearest direct T→T hop along [110], which is sometimes discussed in the physics literature, does not pass through any special symmetry points, and involves a short-cut route through the octahedral site. The direct route passes much closer to one of the selenium sites (vertices) and it is therefore energetically unfavorable.

Table S2. Geometric considerations for different types of hopping in Cu_2Se.

Possible hopping routes	Nearest Cu-Se approach distance, in terms of FCC lattice constant a	Geometry
T-T, hopping along [100]	a / 2√2 = 0.354 a	through tetrahedral edge
T-T, hopping along [110]	a/4 = 0.25 a	No direct path: involves a short-cut through an octahedron
T-O (or O-T) hopping along [111]	a / √6 = 0.408 a	through triangular face
O-O, hopping along [110]	a / 2√2 = 0.354 a	through tetrahedral edge, the same as T-T [100], but in the perpendicular direction

In other words, from a steric point of view, T-O and O-T hops are far more likely than T-T [100] hops, which are in turn more likely than direct T-T [110] hops.

Finally, in the section below we analyze the statistics of finding a vacant tetrahedral site, to which a copper ion can jump. Let us consider non-stoichiometric $Cu_{2-2x}Se$, in which the tetrahedral sites are not all occupied. If any given Cu-ion is going to hop (via an octahedral site) to another tetrahedral site, it can only do so, if the new site is unoccupied. It can jump to any of the four neighboring octahedral which are all unoccupied, but then it has eight options, one for each face of the octahedron:

(a) Jump right back to the tetrahedron, from whence it came
(b) Jump out through one of the three adjacent triangular faces, giving an overall ½ (100)-type hop
(c) Jump out though one of three next-closest triangular faces, giving an overall ½ (110)-type hop
(d) Jump out through the opposite face of the octahedron, giving an overall ½ (111)-type hop

In other words, if the Cu ion makes any given T-O hop, and a fraction x of the tetrahedral sites are unoccupied, the probability of finding a vacant T site to jump onto is 7x (for small x). More precisely, the probability is $1 - (1\text{-}x)^7$. Or generalizing to a shell (or sphere) of n potential hopping sites, the probability, of finding at least a single vacant site onto which it can hop, is $1 - (1\text{-}x)^n$.

But it is more complicated, because the initial T-O hop is one of four such possibilities, and each of these has its own set of (a-d). But some of these go to tetrahedral sites that we have already considered. In other words, if we consider T→O→T hops, there may be two different routes that the Cu-ion can take (via different octahedral). And for T→O→O→T hops it is yet more complicated.

To simplify the analysis, it is useful to disregard the selenium sublattice, and only count through the occupancies of the shells of Cu-neighbors. The Cu ions sit on a simple cubic lattice, with neighboring Cu ions as listed in Table 3. All hops up to third nearest neighbor are possible via a single O site, and the cumulative probability up to the 3rd neighbors is 23 %. Hopping to the 4th NN and above is not possible via a single O site, and for that reason hops to more distant than the 3rd NN are omitted from Table S3.

Table S3. Statistical analysis of the probability of finding a vacancy that is accessible using a T-O transition in Cu_2Se.

Neighbor	Cu-Cu spanning vector (on simple cubic copper lattice)	Accessible through a single octahedral site, T→O→T	Number of neighbors, *n*	Probability of having a neighboring site (in that shell) to hop into, for $Cu_{1.98}Se$ (x = 1% vacancies); $P = 1 – (1-x)^{n}$	Cumulative number of neighbours within a shell, n_S	Probability of having a neighboring site (within that shell) to hop into, for $Cu_{1.98}Se$ (x = 1% vacancies); $P = 1 – (1-x)^{ns}$
1^{st} Nearest-Neighbor	100	yes	6	5.85%	6	5.85%
2_{nd}^{t} Nearest-Neighbor	110	yes	12	11.36%	18	16.55%
3^{rd} NN	111	yes (but only half of them)	8 (only 4 through a single O-site)	7.73%	26 (22)	23.00%

From this analysis, within the range of possible T → O → T hops (through a single octahedron), it is statistically twice as likely to be a net [110]-type hop, as opposed to a net [100]-type hop: 11.36% compared to 5.85% (for a 1% vacancy probability)

SI6. Experimental Thermal Conductivity:

The thermal diffusivity (*D*) was measured by the laser-flash method (Linseis LFA 1000) under vacuum. The assumptions made when using this method include (i) homogeneity and isotropy of the material and (ii) property invariance with temperature within experimental conditions (see ASTM standard E1461 for full detail of technique). The specific heat (C_p) was determined by differential scanning calorimetry (DSC) (Netzsch DSC-204F1-Phoenix calorimeter) under an argon atmosphere with a flow rate of 50 ml/min. The sample density (ρ) was calculated using the measured weight and dimensions. The thermal conductivity (κ) was calculated by

$\kappa = D \times C_p \times \rho$. Note that D is ostensibly depressed during the endothermic α→β phase transition whereas C_p is ostensibly increased. The net result is a spurious value for κ whilst the phase transformation is in progress.

SI7. Technical Details of Neutron Scattering Experiment

To account accurately for the slight Q-dependence (angular dependence) of the resolution function, all data were fitted by convoluting with the true resolution function determined by measuring a vanadium standard. The data on the area detector was also normalized per-pixel to the signal from the vanadium standard. Data were collected at 300, 400, 500, 550 and 675 K. The background signal was subtracted using scans of the empty sample can under identical conditions. To permit analysis of the quasielastic component, the Bragg reflections were excluded by removing the corresponding angular ranges on the detector bank. The remaining data were transformed into S(Q,ω) using a sufficiently coarse Q-resolution such that there are no missing points. Data manipulations and fitting were carried out using the Large Array Manipulation Program (LAMP) [1].

SI8. Details of the quasi-elastic fitting model

This section discusses a general and robust model that can place limits on the diffusion coefficients obtained with QENS, and which is generally suitable for superionic conductors. Although this approach sacrifices a small amount of accuracy, it contains the minimal description of the essential physical processes and can be used to place upper and lower bounds on the diffusion coefficient. There are five distinct steps in the fitting process: 1) selection of of appropriate Q/ω regions 2) establishing the minimal QENS model capturing the two distinct physical processes 3) quantitative fitting 4) extracting the long-range diffusion component 5) placing bounds on the data. Each of these steps is detailed below.

Selection of Q and ω regions for fitting: In a superionic conductor, three types of motion coexist: 1) diffusion of one species, 2) confined diffusion for ions trapped near their stable site undergoing sporadic large displacements, and 3) phonons for the surrounding lattice causing small collective displacements. Disentangling these three factors in a solid-state QENS experiment is non-trivial because the atomic motion seen by neutron scattering in the intensity function $S(Q,\omega)$ is a superposition of all degrees-of-freedom. However, by carefully selecting the ω/Q region, it is possible to select regions where the phonons make virtually no contribution and diffusive (QENS) processes dominate. To be specific, low energy acoustic phonons can be minimized by avoiding the Q-regions corresponding to zone centers. The optical phonons, which are present at all Q, are less of an issue since they generally contribute intensity at $\omega >> 0$ that is easily distinguished from QENS processes ($\omega \sim 0$). However, in rare cases, low-energy optical modes can still provide a broad background signal, which can be mistaken for a broad quasielastic component. Thus, it is advisable to avoid any contribution of optical phonons by disregarding ω energies near to and above the first optical branch. Identifying the strong coherent contributions in the simulated cross-section (e.g. Fig. 6(b)) is a good method to cross-check these choices. Thus, in Cu_2Se, fitting was accomplished by using data for 0.5 Å^{-1} < Q < 1.6 Å^{-1} away from the Brillouin zone centers, and at energies < 5 meV, below the first optical branches. This prevents spuriously inferring a QENS signal from low energy phonons.

Establishing the minimum QENS model: Having restricted the ω/Q range, the next task is to separate the confined and long-range diffusion components via their unique Q dependence and energy-width. Confined diffusion involves the atom jumping around sporadically, but always eventually returning to the same site, owing to confinement. This generates an elastic component, together with a QENS component. The latter is generally tied to higher frequency vibrations thus giving a broader E-width described by a FWHM (Γ >2-10 meV) with an FWHM (Γ) that is independent of Q (to a very good approximation). In contrast, long-range diffusion involves atoms leaving their initial site, and travelling long distances in the lattice. This leads to a Q-dependent FWHM (Γ that increases as Q^2, at low momentum transfer, with a Γ that is typically in the range of 0.01 - 2 meV below Q = 2.0 Å^{-1}. In general the two types of diffusion have very different time-scales, and long-range diffusion involves lower frequency events as many trial hops occur before each long-range hop. To account for these two types of motion, it is generally necessary to use multiple Lorentzians to fit the QENS data. As shown in Figure S3, models fitting to a single Lorentzian yielded unsatisfactory results are reported by others [3, 8, 9], since it yields a convoluted average of the two processes, and the diffusion coefficient obtained will be unreliable. The single Lorentzian fit tends to overestimate the intensity near the elastic line and also fails to capture the higher energy region, leading to a large residue and a poor figure of merit (χ^2). As discussed above, there is also good physical justification for expecting at least two components in the self-correlations, reflected in two (or more) distinct

Lorentzian contributions to the QENS. In the case of Cu_2Se, two Lorentzians are sufficient to fit the entire accessible Q/E range, as demonstrated in the manuscript and in Figure S3 below. To reliably separate the two processes, it is advantageous to constraint the fitting as described in the next section.

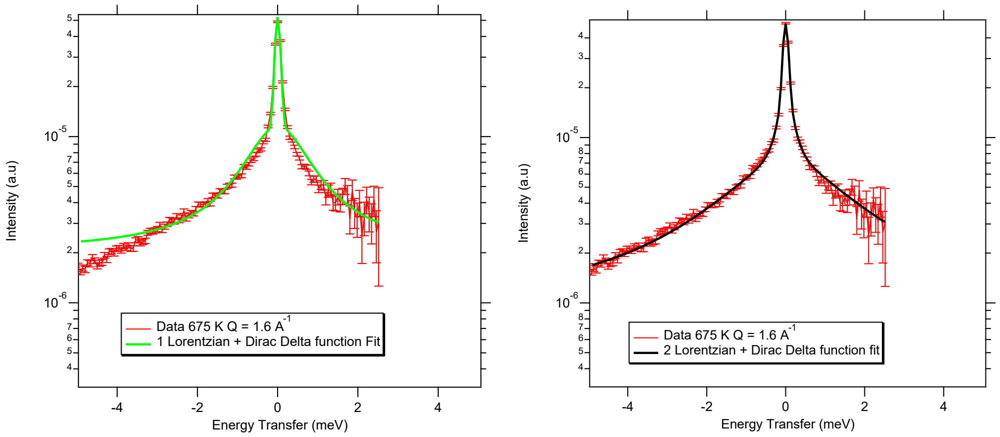

Figure S3. Comparison of QENS fits using a single Lorentzian (left) or 2 Lorentzians (right) to describe the quasi-elastic contribution.

Quantitative fitting expression: The minimal model that describes the QENS data in the Cu_2Se superionic system is the δ-function elastic peak, in combination with two Lorentzian quasielastic components:

$$S(Q,\omega) = A(Q)\delta(\omega) + \big(1 - A(Q)\big)L_1(\omega) + L_2(\omega, Q) \qquad (3)$$

The first Lorentzian L_1 represents the localized, confined "jump-diffusion" around an average position:

$$L_1 = \frac{\left(\frac{\Gamma_1}{2}\right)^2}{\pi\left[\omega^2+\left(\frac{\Gamma_1}{2}\right)^2\right]} \qquad (4)$$

It is well known that this type of confined diffusion leads to a FWHM (Γ_1) that is essentially independent of Q^2 [30]. As the particle sporadically returns to its original position, there is an elastic incoherent structure factor contribution given by *A(Q)* which depends on the confinement geometry. As a first approximation, the relation for a sphere with radius *a* can be used since the deviation from this will be small at low Q for any more complex geometry [30]:

$$A\,(Q) = \left[\frac{3j_1\,(Qa)}{Qa}\right]^2 \tag{5}$$

where j_1 is the n=1 spherical Bessel function [31, 32]. In practice the fitting procedure can also leave $A(Q)$ as a free parameter determined at each Q. This is the approach used in our work. Figure S4 compares the measured EISF with Equation 5 for the Cu_2Se data at 675 K showing the results are very similar. The second Lorentzian accounts for long-range diffusion and has a Q-dependent energy-width (Γ_{D}):

$$L_2 = \frac{\left(\frac{\Gamma_{\mathrm{D}}}{2}\right)^2}{\pi(\omega^2+\left(\left(\frac{\Gamma_{\mathrm{D}}}{2}\right)\right)^2} \tag{6}$$

Thus, unlike Γ_1 which is common to all Q points, Γ_{D} is a free parameter determined at each Q value. It is important to recognize that this model is different from those of both Danilkin *et al.* [8] and Voneshan *et al.* [3] because it explicitly models the confined diffusion as a Lorentzian with Q-independent width. The fits to this simple model are excellent, as shown in Figs. 7(a) and 7(b) in the main manuscript. The fitting was achieved using a 2D fit to minimize the global figure-of-merit χ^2 by iterating Γ_1 through a set of values whilst allowing Γ_D to fit freely at each value. The results are discussed in the main manuscript.

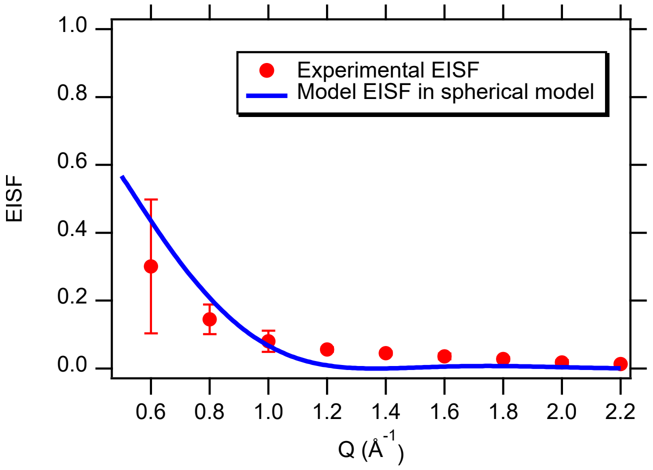

Figure S4. Measured EISF compared with the EISF estimated from a simple spherical model with a = 3.3 ± 0.2 Å

Extracting the long-range diffusion component: Provided the localized QENS component is accounted for properly, as described above, the Q-dependence of the second Lorentzian component is the key to detecting the diffusion coefficients. Different types of long-range diffusion (Hall-Ross, Fickian and Chudley Elliot) will lead to some variation in the Q-dependence at higher Q. In the case of the Cu_2Se system, neither the Fickian model (which describes the free diffusion such as in water), nor the Hall-Ross Model (which describes a fully random set of short-range of jumps with a Gaussian distribution) capture the Q-dependency of the Γ_D. Instead, in agreement with past work [3], the Q-dependence is well described by the Chudley-Elliot (CE) model which describes long-range diffusion by discrete jumps between distinct crystallographic sites with a characteristic spacing. In the CE model, the FWHM from the diffusive component is:

$$\Gamma_D = \frac{2\hbar}{\tau}\left(1 - \frac{\sin(Qd)}{Qd}\right) \tag{2}$$

where τ is the hopping time, and d is the hopping length and the diffusion coefficient is $d^2/6\tau$. Fig. 7 (a) shows a plot of the behavior of the CE model, within the experimental ω/Q range using d = 2 Å and d = 3 Å corresponding to T↔O and T↔T transitions respectively. The most convincing method to clarify whether one of the latter hopping types dominates would be to observe a maximum in Γ_D at $Qd = \frac{3\pi}{2}$ and the first minima in at $Qd = \frac{5\pi}{2}$. However, this is outside of the available experimental Q-range in Cu_2Se, so more approximate methods are needed. At very low Q, by taking the Taylor series of the CE model, one can see that $\Gamma_D \sim 2\hbar\, d^2/\tau$, and thus d^2 and τ parameters cannot be independently determined with a high level of precision, although the diffusion coefficient $d^2/6\tau$ is well resolved and for this reason the d = 2Å and d = 3Å collapse onto each other at low Q in Fig. 7. Meanwhile, at the other limit of extremely high Q, the CE model approaches a constant value of $\frac{2\hbar}{\tau}$ that is independent of d. The accessible Q-range in Cu_2Se is somewhere between these limits, where the models are expected to show differences, albeit with a FWHM that approaches the experimental resolution (S4). For this reason, it is advantageous to establish the minimal model that can fit the data, and then use this to place broad upper and lower limits on the diffusion coefficients.

.

Placing bounds on the data: There are solid physical grounds to expect both O↔T and T↔T hops, but from the QENS data alone it is difficult to separate these two types of motion as both have similar jump lengths and hopping timescales and so will yield a similar Γ_D, thus potentially appearing as a single Lorentzian. As the diffusion coefficient determination depends, to some extent the ratio of O↔T to T↔T hops, we have developed a procedure to place bounds on the data assuming some distribution of hops. We assume that for two Lorentzians with the same width, within or near the resolution limit, these will appear as a single Lorentzian with an intensity that is the average of the two constituent Lorentzians, where the area under each Lorentzian is weighted by the fraction of each component. This allows assumption means that, for any fraction of different hops, the experiment will measure the intensity-weighted average (shown for example in Fig.S4) which always lies in the area between two single-Lorentzian limits obtained by assuming that 100% of either O↔T or T↔T hops. Importantly, although the true value will be in this region, it may not necessarily appear at the mid-point, even if the ratio was 50:50 However, provided the single-Lorentzian data bounds all of the data, the true average will be included somewhere in the area bounded by the two curves. This allows one to place upper and lower limits.

To illustrate this, Fig. S4 (a) shows a plot of the behavior of the CE model, within the experimental ω/Q range using d = 2 Å and d = 3 Å corresponding to T↔O and T↔T transitions respectively.

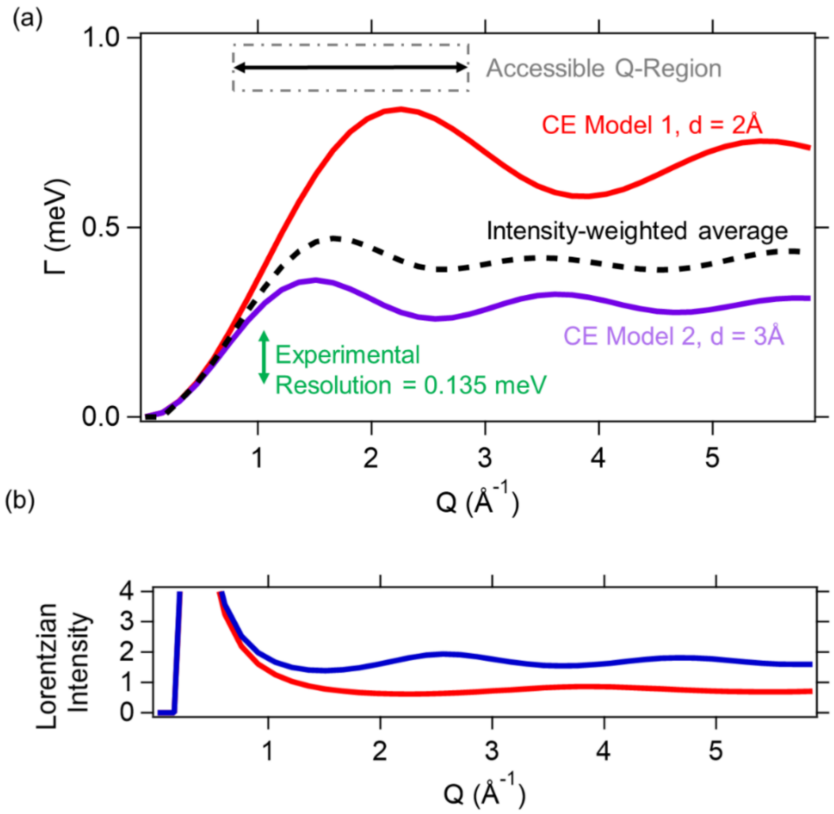

Fig. S5. (a) Plots of the Lorentzian width for the Chudley-Elliot model with two sets of parameters with d = 2 Å and d = 3 Å, chosen to give the same diffusion coefficients $d^2/6t$. The region of Q/E accessible in the experiment is shown in shaded region, along with the energy resolution. Within resolution the two models will have the same FWHM. Assuming both types of hops coexist with the same likelihood, the dotted line shows the apparent average width weighted by the intensity of each Lorentzian. (b) The apparent intensity of each Lorentzian in the model assuming that the intensity is inversely proportional to the FHWM so that the integrated area under each Lorentzian is constant.